Photodissociation spectroscopy and dynamics of the CH₂CFO radical

Alexandra A. Hoops, Jason R. Gascooke,[a] Kathryn E. Kautzman, Ann Elise Faulhaber, and Daniel M. Neumark[b]
Department of Chemistry, University of California, Berkeley, California 94720 and Chemical Sciences Division, Lawrence Berkeley National Laboratories, Berkeley, California 94720

The photodissociation spectroscopy and dynamics resulting from excitation of the $\tilde{B}\,^2A'' \leftarrow \tilde{X}\,^2A''$ transition of CH_2CFO have been examined using fast beam photofragment translational spectroscopy. The photofragment yield spectrum reveals vibrationally resolved structure between 29 870 and 38 800 cm^{-1}, extending $\sim$6000 cm^{-1} higher in energy than previously reported in a laser-induced fluorescence excitation spectrum. At all photon energies investigated, only the CH_2F+CO and $HCCO+HF$ fragment channels are observed. Both product channels yield photofragment translational energy distributions that are characteristic of a decay mechanism with a barrier to dissociation. Using the barrier impulsive model, it is shown that fragmentation to CH_2F+CO products occurs on the ground state potential energy surface with the isomerization barrier between CH_2CFO and CH_2FCO governing the observed translational energy distributions. © *2004 American Institute of Physics.* [DOI: 10.1063/1.1691016]
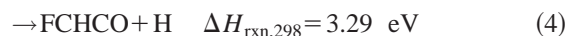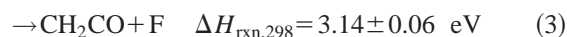
I. INTRODUCTION

The CH_2CFO radical belongs to a class of halogen-substituted vinoxy radicals that has been receiving increased attention in the past several years, in part to understand how these species differ from the well-characterized vinoxy radical. Recently, the spectroscopy of not only CH_2CFO,[1-3] but also *cis-* and *trans*-CHFCFO,[4] *cis*-CHClCFO,[4] and *cis-* and *trans*-CHClCHO[5] has been investigated. In the current work, we report the first experimental investigation of the photodissociation dynamics of the CH_2CFO radical. We determine the photofragment yield spectrum, identify the products, and measure the translational energy distribution for each product channel.

CH_2CFO has three low-lying excited states accessible from its ground $\tilde{X}\,^2A''$ state; the $\tilde{A}\,^2A'$ state is predicted to lie in the near infrared, while the $\tilde{B}\,^2A''$ and $\tilde{C}\,^2A'$ states are in the ultraviolet.[3] Several recent experimental and theoretical studies[1-3] have focused on the $\tilde{B}\,^2A'' \leftarrow \tilde{X}\,^2A''$ transition, for which $T_0 = 29\,867\,cm^{-1}$ (3.70 eV).[2] Furubayashi *et al.*[1] reported a vibrationally-resolved laser-induced fluorescence (LIF) excitation spectrum of CH_2CFO over the range of 29 870–32 570 cm^{-1}. The origin band of this transition was partially rotationally resolved by Wright and Dagdigian.[2] Calculations of optimized geometries and vibrational frequencies for the $\tilde{X}$ and $\tilde{B}$ states of CH_2CFO using the complete active space self-consistent field (CASSCF) method established that the observed band was the result of exciting the $\tilde{B}$ state.[3] Spectral assignments, aided by measured dispersed fluorescence spectra, revealed excitation of the ν_3 (C–O stretch), ν_4 (CHH scissor), ν_5 (C–F stretch), ν_6 (CH₂

rock), ν_7 (C–C stretch), ν_8 (FCO bend), and ν_9 (CCO bend) modes of the $\tilde{B}$ state.[1,6]

The LIF study by Furubayashi *et al.*[1] yielded a fluorescence lifetime of 81 ns for the 0_0^0 and 9_0^1 transitions. A lower lifetime of 49 ns was seen for the 3_0^1 transition, which lies 1790 cm^{-1} above the origin. These lifetimes and the reduced intensity for the 3_0^1 transition relative to the 0_0^0 transition led the authors to suggest that the $v_3' = 1$ level predissociates. At the photon energies used to excite the $\tilde{B}\,^2A'' \leftarrow \tilde{X}\,^2A''$ transition, several dissociation pathways are thermodynamically accessible:

$$CH_2CFO \rightarrow CH_2F + CO \quad \Delta H_{rxn,298} = 1.33 \pm 0.11 \text{ eV} \quad (1)$$

$$\rightarrow HCCO + HF \quad \Delta H_{rxn,298} = 1.84 \pm 0.07 \text{ eV} \quad (2)$$

$$\rightarrow CH_2CO + F \quad \Delta H_{rxn,298} = 3.14 \pm 0.06 \text{ eV} \quad (3)$$

$$\rightarrow FCHCO + H \quad \Delta H_{rxn,298} = 3.29 \text{ eV} \quad (4)$$

$$\rightarrow CHCOH + F \quad \Delta H_{rxn,298} = 4.08 \pm 0.06 \text{ eV} \quad (5)$$

$$\rightarrow FCCH + OH \quad \Delta H_{rxn,298} = 4.52 \pm 0.65 \text{ eV}. \quad (6)$$

The heats of formation used to obtain the heats of reaction for channels (1)–(3), (5), and (6) are listed in Table I, while the heat of reaction for channel (4) is obtained from the theoretical work by Cao *et al.*[7] The energy level diagram for CH_2CFO and these product channels is presented in Fig. 1.

The role CH_2CFO as a reactive intermediate has also be studied. The $CH_2CO + F$ reaction has been investigated both in a flow reactor[17-19] and theoretically.[20] Grußdorf *et al.*[19] have shown that the main products are $CH_2F + CO$ (87%) with a smaller contribution from $HCCO + HF$ (5%). The

a)Current address: Department of Chemistry, Adelaide University, South Australia 5005, Australia.
b)Author to whom correspondence should be addressed. Electronic mail: dan@radon.cchem.berkeley.edu

TABLE I. Heats of formation for species relevant to the dissociation of CH$_2$CFO.

Species	$\Delta H_{f,298}$ (eV)	Reference	Species	$\Delta H_{f,298}$ (eV)	Reference
F	0.8228 ± 0.0031	8	HCCO	1.83 ± 0.03	11
HF	-2.825 ± 0.008	8	FCCH	1.30 ± 0.65	8
OH	0.386 ± 0.003	9	CH$_2$CO	-0.5139 ± 0.0091	12
CO	-1.146 ± 0.002	8	CHCOH	0.431	13
CH$_2$F	-0.35 ± 0.09	10	CH$_2$CFO	$-2.83 \pm 0.06^{\text{a}}$	

[a]Value calculated using the gas phase acidity of CH$_3$CFO (Ref. 14), $\Delta H_{f,298}$ (H) (Ref. 8), $\Delta H_{f,298}$ (CH$_3$CFO) (Ref. 15), and electron affinity of CH$_2$CFO (Ref. 16).

CH$_2$F+CO channel was attributed to a long-lived, vibrationally excited intermediate,[17] either the FCH$_2$C=O or CH$_2$C(=O)F radical,[20] while the HCCO+HF channel was attributed to direct H-atom abstraction.[18,19] Recently, a detailed theoretical study of the C$_2$H$_2$FO radical potential energy surface by Cao *et al.*[7] at the B3LYP/6-311G** and CCSD(T)/6-311G** levels yielded barrier heights for numerous ground state dissociation pathways. Additionally, this work showed that the transition states (TS) leading to channels (1), (3)–(6) lie below the excitation energies involved in the $\widetilde{B}\,^2A'' \leftarrow \widetilde{X}\,^2A''$ transition. No transition states were reported for the dissociation of CH$_2$CFO to HCCO+HF products.

In contrast to CH$_2$CFO, the vinoxy radical, CH$_2$CHO, has been studied to a great extent both experimentally and theoretically. The vinoxy radical has two observed excited electronic states, which have been examined by absorption,[21] hole-burning spectroscopy,[22] LIF,[23–27] photodissociation,[28] and anion photoelectron spectroscopy.[29] Spectroscopic investigations of the $\widetilde{B}\,^2A''$ state reveal that at energies approximately 1400 cm^{-1} above the origin, fluorescence is quenched by predissociation.[21–26,28] In fact, all vibrational levels of the CH$_2$CHO $\widetilde{B}\,^2A''$ state predissociate to CH$_3$+CO and CH$_2$CO+H photoproducts with a branching ratio estimated to be 1:4.[28] Both product channels were attributed to dissociation on the ground state potential energy surface over a barrier following rapid internal conversion (IC) from the $\widetilde{B}$ state. Based on calculations of stationary points[28] and potential energy curves along the C–C torsional coordinate,[30] a two-step internal conversion mechanism, $\widetilde{B}\,^2A'' \rightarrow \widetilde{A}\,^2A' \rightarrow \widetilde{X}\,^2A''$, was proposed as the pathway between the excited and ground states.[28] A more complete mechanism was provided in recent calculations by Matsika and Yarkony,[31] who showed that IC from the $\widetilde{B}$ to $\widetilde{A}$ state takes place via an avoided crossing of nonplanar symmetry after overcoming a barrier of $\sim$2000 cm^{-1} on the $\widetilde{B}$ state potential energy surface, with subsequent IC to the ground state occurring through a conical intersection.

In the present study, dissociation from the $\widetilde{B}\,^2A''$ state of CH$_2$CFO has been investigated. Vibrationally resolved structure of the $\widetilde{B}\,^2A'' \leftarrow \widetilde{X}\,^2A''$ transition is observed in the photofragment yield spectrum, extending $\sim$6000 cm^{-1} further to the blue than the previous LIF spectrum.[1] In addition, the photodissociation dynamics have been examined with a newly implemented coincidence imaging detection scheme.[32] The photofragment mass ratios obtained illustrate that the CH$_2$F+CO and HCCO+HF channels are present, while the F-loss channel, which is analogous to the H-loss channel observed in vinoxy, is absent. Furthermore, the fragment translational energy and angular distributions, as well as product channel branching ratios, provide insight into the decay mechanism of CH$_2$CFO.

II. EXPERIMENT

The current photodissociation experiments were performed on our fast beam photofragment translational spectrometer, Fig. 2. As the instrument has been described in detail previously,[28,32–34] only a brief account will follow.

Rotationally and vibrationally cooled CH$_2$CFO$^-$ is produced by supersonically expanding a dilute mixture of acetyl fluoride (99% Aldrich) in He (0.5%–2% CH$_3$CFO total) through a pulsed piezoelectric valve/electrical discharge source.[35] A 1 keV electron beam intersects the free jet expansion downstream of the valve orifice. By using a mixture of acetyl-d_3 fluoride in He (<0.5% CD$_3$CFO total), CD$_2$CFO$^-$ is generated in an analogous manner. Deuterated acetyl fluoride is synthesized by reacting a heated mixture of KF (99% Aldrich) and acetic-d_3 acid-d (99.5% Aldrich) with acetyl-d_3 chloride (99+% Aldrich).[36]
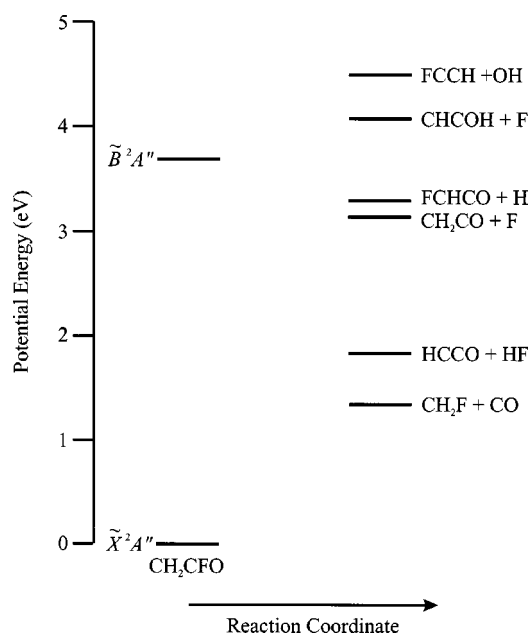

FIG. 1. Energy level diagram for the CH$_2$CFO radical indicating the position of CH$_2$CFO electronic energy levels relative to the asymptotic energies of the fragment channels.
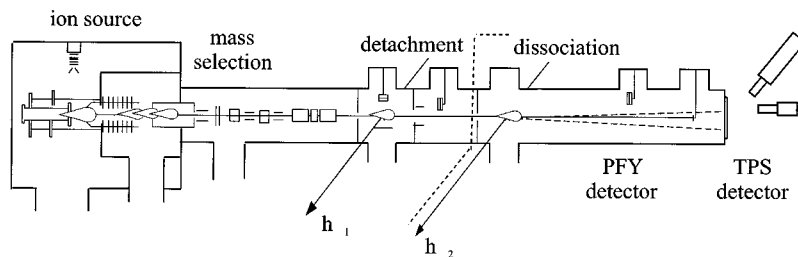
FIG. 2. Fast beam photofragment translational spectrometer.

The resulting molecular beam passes through a skimmer into a differentially pumped region, and anions in the beam are accelerated to a laboratory beam energy of 8 keV. The anions are mass-selected using a Bakker time-of-flight (TOF) mass spectrometer, which imparts negligible kinetic energy spread to the ion beam.[37,38] An excimer-pumped dye laser is used to photodetach an electron from CH_2CFO^-, and any remaining ions are deflected out of the beam path. Based on the adiabatic electron affinity of CH_2CFO, 2.195 eV,[16] and the measured and calculated vibrational frequencies of CH_2CFO in the ground state,[1] a photodetachment energy of 2.234 eV was chosen to generate $CH_2CFO(\tilde{X}\,^2A'')$ with minimal vibrational excitation.

The fast radicals produced by photodetachment intersect the frequency doubled output of a second excimer-pumped dye laser with a bandwidth of 0.3 cm^{-1}. Resulting photofragments are detected directly by one of two microchannel plate (MCP) detectors, the photofragment yield (PFY) or the time- and position-sensing (TPS) detector. Beam blocks in front of both detectors prevent undissociated radicals from impacting the MCPs. Consequently, any observed signal is due to the recoiling photofragments.

Two types of experiments are performed to characterize the photodissociation of CH_2CFO: First, by scanning the dissociation laser energy and measuring the total flux of photofragments arriving at the retractable PFY detector, one obtains a photofragment yield spectrum. In the current study, the dissociation of CH_2CFO from 29 680 to 40 000 cm^{-1} is

investigated. Second, the dissociation laser can be tuned to a specific photon energy and the fragments detected in coincidence with the TPS detector, Fig. 3. The TPS detector in use is a coincidence imaging detector based on the design by Amitay and Zajfman[39] and has been described in depth previously.[32] In this detection scheme, recoiling photofragments strike a MCP detector coupled to a phosphor screen. Emission from the phosphor screen is reflected by a dichroic beamsplitter to a multianode photomultiplier tube (PMT) and transmitted to a charge-coupled device (CCD) camera via an image intensifier. The position of the impact is obtained from the CCD camera, while the PMT provides timing information and a crude estimation of the position. For each dissociation event, the photoproduct arrival times and positions yield the masses of the fragments, center-of-mass translational release E_T, and recoil angle θ. Based on the photofragment translational energy $P(E_T)$ distribution resulting from the dissociation of $O_2 B\,^3\Sigma_u^-\,(v'=7)$, the current translational energy resolution of this arrangement is $\Delta E_T/E_T \approx 0.7\%$.[32]

The presence of a beam block in the center of the TPS detector reduces the acceptance by the detector for those fragments that have low translational energy or values of θ close to 0° or 180° with horizontally polarized laser light, while fragments of high translational energy with θ close to 90° miss the detector entirely. These effects are accounted for by normalizing the raw translational energy distributions with a detector acceptance function (DAF),[34] and all data
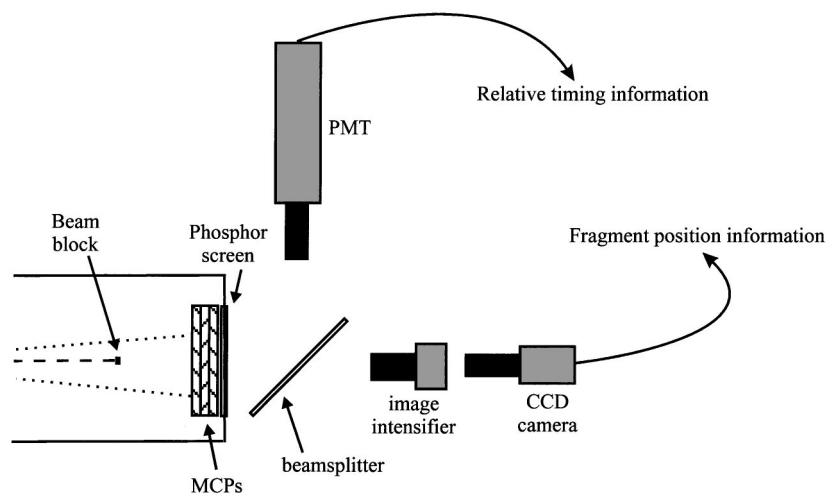

FIG. 3. Schematic diagram of the coincidence imaging detector. The paths of the photofragments and parent radical are represented by dotted and dashed lines, respectively.
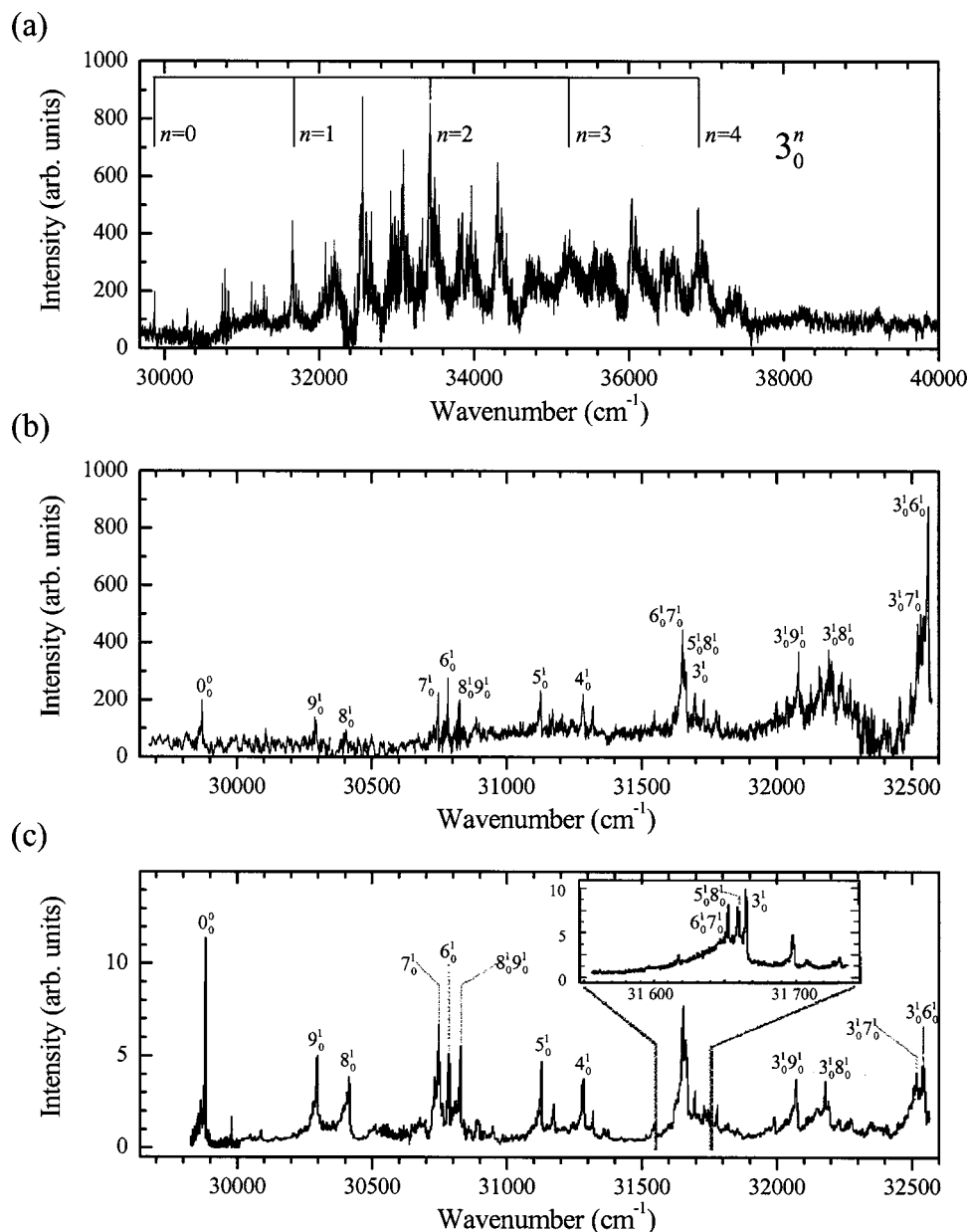
FIG. 4. Photofragment yield spectrum of CH$_2$CFO: (a) 29 680 to 40 000 cm^{-1}, (b) expanded view 29 680 to 32 570 cm^{-1}, and (c) LIF excitation spectrum adapted from Ref. 1.

presented here has been corrected with the DAF. It should be noted that in the current results, inclusion of the DAF does not significantly alter the photofragment translational energy distributions.

III. RESULTS

A. Photofragment yield spectrum

The PFY spectrum for the $\tilde{B}\,^2A'' \leftarrow \tilde{X}\,^2A''$ band of the CH$_2$CFO radical from 29 680 to 40 000 cm^{-1} is presented in Fig. 4(a). The spectrum above 32 570 cm^{-1} has not been previously reported. The PFY spectrum shows extended vibrational progressions in the $\tilde{B}$ state with linewidths of 5–10 cm^{-1} near the origin that widen to 30–70 cm^{-1} as the excitation energy is increased. The features remain at least partially vibrationally resolved up to ~1 eV above the origin.

The linewidths near the origin are presumably from rotational structure that is unresolved under our experimental conditions.[2]

Figure 4(b) shows an expanded view of the PFY spectrum from 29 680 to 32 570 cm^{-1}, while Fig. 4(c) shows the LIF excitation spectrum[1] in the same region. The peak positions in the two spectra agree, but the patterns of intensities differ. The origin of the $\tilde{B}\leftarrow\tilde{X}$ band in the LIF excitation spectrum is the most intense transition, while in the PFY spectrum the origin is rather weak and several bands at higher excitation energy are more intense, with the $3^1_0 6^1_0$ combination band being the most intense feature in Fig. 4(b). This general trend indicates that dissociation becomes more competitive with fluorescence as the excitation energy increases. The peak positions, assignments, and intensities can be found in Table II. Assignment of the peaks will be dis-

TABLE II. Peak positions (cm^{-1}), relative intensities, and vibrational assignments for the PFY spectrum of CH$_2$CFO.

Wavelength	Intensity	Assignment	Wavelength	Intensity	Assignment	Wavelength	Intensity	Assignment
29 870[a]	23	0_0^0	31 999	22	$5_0^1 7_0^1$	33 440[a]	85	3_0^2
30 291[a]	15	9_0^1	32 038	24	$5_0^1 6_0^1$	33 491	67	
30 404[a]	11	8_0^1	32 081	41	$3_0^1 9_0^1$	33 549	57	
30 746[a]	26	7_0^1	32 125	29	$6_0^2 9_0^1$	33 800	52	
30 781[a]	32	6_0^1	32 160	36	$7_0^2 8_0^1$	33 847	54	
30 824	22	$8_0^1 9_0^1$	32 193	43	$3_0^1 8_0^1$	33 907	44	
31 125[a]	27	5_0^1	32 237	34	$7_0^1 8_0^1 9_0^1$	33 952	50	
31 170	19	$7_0^1 9_0^1$	32 538[a]	53	$3_0^1 7_0^1$	33 966	65	$3_0^2 8_0^1$
31 205	17	$6_0^1 9_0^1$	32 561[a]	100	$3_0^1 6_0^1$	34 020	47	
31 245	15	$8_0^1 9_0^2$	32 606	54	$3_0^1 8_0^1 9_0^1$	34 283	53	$3_0^2 7_0^1$
31 282	25	4_0^1	32 650[a]	43		34 304[a]	74	$3_0^2 6_0^1$
31 292	14	$7_0^1 8_0^1$	32 672[a]	54	4_0^2	34 360	52	
31 319	20	$6_0^1 8_0^1$	32 919	58	$3_0^1 5_0^1$	34 421	46	
31 354	11	$8_0^2 9_0^1$	32 940	49	$3_0^1 7_0^1 9_0^1$	34 718	37	
31 547	19	$5_0^1 9_0^1$	32 975	53	$3_0^1 6_0^1 9_0^1$	34 837	36	
31 621	19	7_0^2	33 021	51	$3_0^1 8_0^1 9_0^2$	35 176	45	3_0^3
31 651[a]	51	$6_0^1 7_0^1$	33 069	65	$3_0^1 4_0^1$	35 232	47	3_0^3
31 658	39	$5_0^1 8_0^1$	33 079	55	$3_0^1 7_0^1 8_0^1$	36 036[a]	60	$3_0^3 7_0^1,\ 3_0^3 6_0^1$
31 664[a]	34	3_0^1	33 090	79	$3_0^1 6_0^1 8_0^1$	36 085	53	
31 697	26	6_0^2	33 140	41		36 435	37	
31 730	23	$6_0^1 8_0^1 9_0^1$	33 331	52	$3_0^1 5_0^1 9_0^1$	36 565	37	
31 776	18	$8_0^2 9_0^2$	33 422	85	$3_0^1 6_0^1 7_0^1$	36 892[a]	55	$3_0^3 6_0^1 7_0^1,$
31 818	14	$7_0^1 8_0^2$	33 431	97	$3_0^1 5_0^1 8_0^1$			$3_0^3 5_0^1 8_0^1,\ 3_0^4$

[a]Transitions for which photofragment translational energy distributions were obtained.

cussed in Sec. IV A. Finally, fundamental vibrational frequencies for the $\widetilde{B}$ state obtained in the current investigation are in close agreement with those measured in the LIF study, Table III.

B. Product mass channels and translational energy distributions

Figure 1 shows that dissociation channels (1)–(4) are accessible at the origin of the $\widetilde{B}\leftarrow\widetilde{X}$ transition, with the remaining channels (5)–(6) becoming energetically accessible over the range of photon energies spanned in Fig. 4(a). The photofragment masses for each dissociation event are determined by conservation of momentum in the center-of-mass frame. Figure 5 shows the product mass distribution when the 3_0^1 transition at 31 666 cm^{-1} (3.926 eV) is excited. Only two mass channels are observed, CH$_2$F+CO and HCCO+HF, as shown by the solid curve in Fig. 5; the same mass channels are observed at all photon energies. In order to confirm the mass assignments, CD$_2$CFO was dissociated at 31 640 cm^{-1} (the 3_0^1 transition[6]). The resulting mass spectrum is depicted by the dotted curve in Fig. 5. The CD$_2$CFO photofragment mass distribution is clearly shifted by 1 amu from that of CH$_2$CFO in the regions corresponding to HF/DF and HCCO/DCCO products and by 2 amu in the region of CH$_2$F/CD$_2$F, thereby verifying that the two principal dissociation channels are channels (1) and (2). Due to its large photofragment mass ratio, channel (4), CHFCO+H, cannot be detected in the current experiment, and no evidence of channels (3), (5), or (6) is observed.

After identifying the fragment masses, the photofragment translational energy and angular distributions[40] are calculated from the coincidence data for each product channel.

$P(E_T)$ distributions for the CH$_2$F+CO and HCCO+HF channels have been obtained at 16 photon energies within the $\widetilde{B}\leftarrow\widetilde{X}$ band and several of the distributions are displayed in Figs. 6 and 7. The maximum kinetic energy release, $E_T^{\max}$, as determined using the heats of reaction for channels (1) and (2), is marked by arrows in the figures. The distributions for both channels are peaked at approximately 0.5 eV, significantly away from $E_T^{\max}$. Furthermore, no appreciable variation correlating to photon energy or vibrational mode probed is observed in the $P(E_T)$ distributions, except for a slight widening of the features with increased photon energy. The angular distributions are isotropic at all excitation energies for both dissociation channels.

The branching fractions for the two observed mass channels have been calculated at all photon energies investigated and are presented in Fig. 8. A clear dependence between branching fraction and photon energy is revealed with a shift in primary dissociation channel from CH$_2$F+CO to HCCO+HF as the excitation energy is increased. As with the $P(E_T)$ distributions, the branching fractions appear to be independent of vibrational mode excited.

IV. ANALYSIS

A. Photofragment yield spectrum

Assignment of the observed features in the PFY spectrum, Table II, is aided by the previously reported LIF excitation spectrum.[1,6] In that work, peaks in the LIF excitation spectrum were identified based on dispersed fluorescence
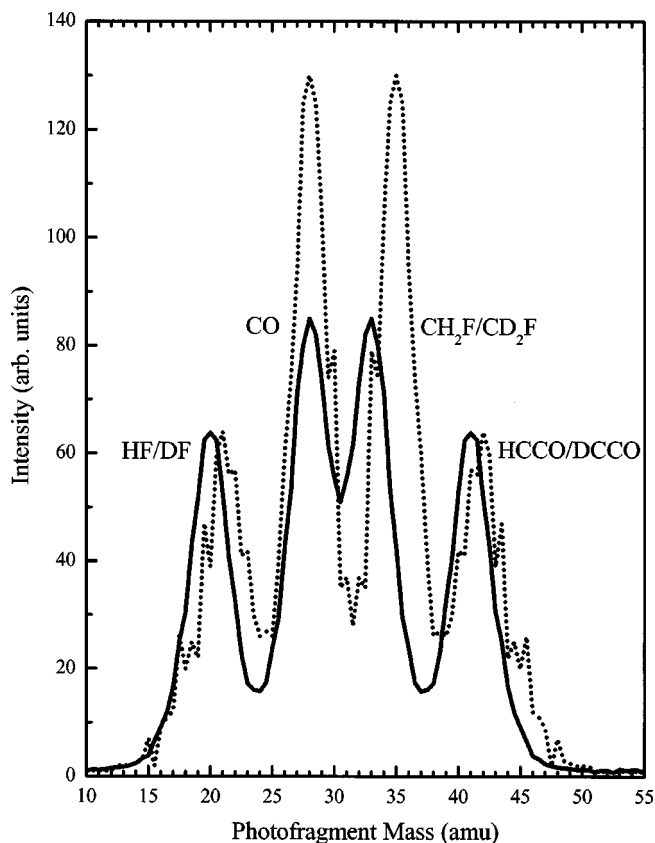
J. Chem. Phys., Vol. 120, No. 18, 8 May 2004

Photodissociation of the CH$_2$CFO radical   8499

FIG. 5. Photofragment mass distribution for the 3_0^1 transition of CH$_2$CFO (31 697 cm^{-1}) and CD$_2$CFO (31 636 cm^{-1}), solid and dotted curves, respectively.
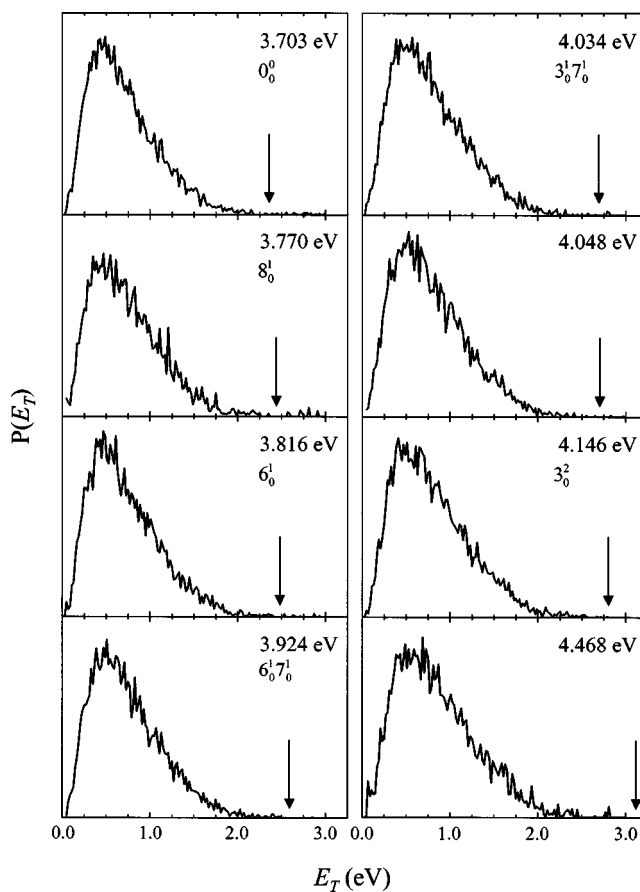

FIG. 6. Photofragment translational energy distributions for CH$_2$F+CO products. Photon energy and vibronic transition, when known, are provided and E_T^{max} is indicated by arrows.

spectra acquired from excitation of the major bands of the $\widetilde{B}$ state. The wavelengths of the features observed in the PFY spectrum are in close agreement with those present in the LIF spectrum [see Figs. 4(b), 4(c)], and accordingly all assignments in the region of 29 680 to 32 570 cm^{-1} are identical to those of the LIF spectrum. From these assignments, the fundamental vibrational frequencies are obtained for the $\widetilde{B}$ state, Table III.

As illustrated in Table II, the PFY spectrum shows single excitation of the ν_3, ν_4, ν_5, ν_6, ν_7, ν_8, and ν_9, modes, all of which are totally symmetric, as well as numerous combination bands. Only the ν_3 mode exhibits an extended progression [see comb in Fig. 4(a)], which is consistent with calculations demonstrating that the primary geometry change between the $\widetilde{X}$ and $\widetilde{B}$ states is elongation of the CO bond.[3] In fact, nearly all the new features in the PFY spectrum, i.e., those beyond 32 570 cm^{-1}, are combination or overtone bands involving the ν_3 mode. For example, the triplet of closely spaced peaks in the LIF spectrum from 31 651 to 31 664 cm^{-1} was attributed to the $6_0^1 7_0^1$, $5_0^1 8_0^1$, and 3_0^1 transitions, and we assign a similar triplet in the PFY spectrum from 33 422 to 33 440 cm^{-1} to the $3_0^1 6_0^1 7_0^1$, $3_0^1 5_0^1 8_0^1$, and 3_0^2 transitions.

The peak assignments in Table II are supported by a simulation using a Dunham-type expansion,

$$E_{\text{Dun}} = \sum_i \omega_i v_i + \sum_{i \leqslant j} x_{ij} v_i v_j + \sum_{i \leqslant j \leqslant k} y_{ijk} v_i v_j v_k, \quad (7)$$

where E_{Dun} is the predicted energy of the transition with v_i quanta of excitation in ν_i. The harmonic frequencies, ω_i, and anharmonic constants, x_{ij} and y_{ijk}, are determined from the spectrum. In order to achieve agreement between the calculated and observed peak positions, anharmonic constants on the order of 0–10 cm^{-1} were included, with the deviations between the two values increasing with photon energy. Consequently, several of the peaks listed in Table II are attributed to more than one transition, as any one of the assignments is possible, and there are two features that are candidates for the 3_0^3 transition. Spectral congestion precludes the identification of all peaks in the PFY spectrum. Furthermore, the CH$_2$ symmetric and asymmetric stretching modes, which were not energetically accessible in the LIF study, could not be differentiated from combination bands in the current PFY spectrum.

B. *Ab initio* calculations

The previous *ab initio* calculations by Cao *et al.*[7] indicated that the dissociation process of CH$_2$CFO→CH$_2$F+CO involves the ground states of both CH$_2$CFO and CH$_2$FCO, as well as the isomerization barrier between the two species and the transition state leading directly to CH$_2$F+CO products. In order to characterize this reaction more completely, we have calculated the structures, energies, and vibrational frequencies of these four stationary
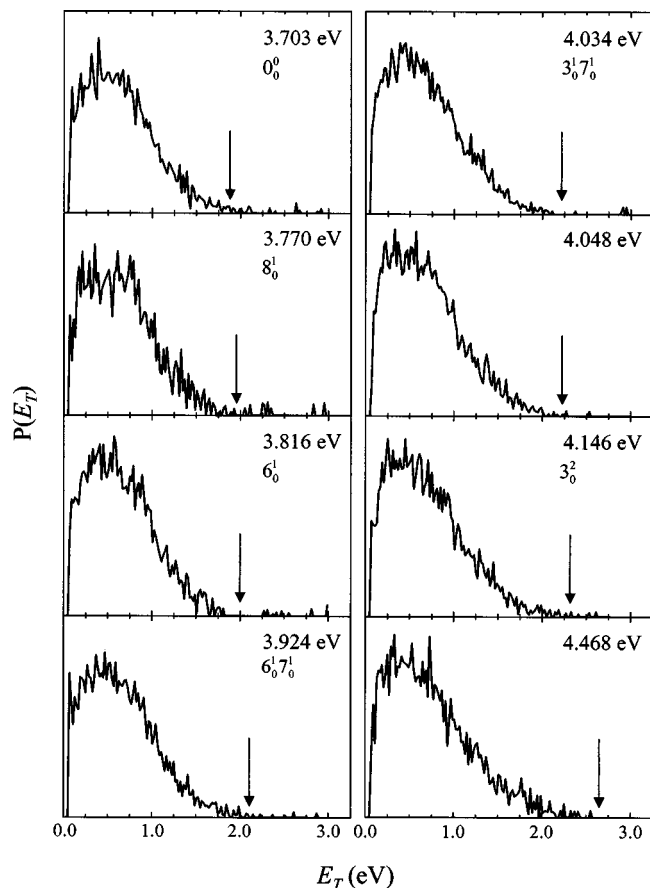
FIG. 7. Photofragment translational energy distributions for HCCO+HF products. Photon energy and vibronic transition, when known, are provided and E_T^{max} is indicated by arrows.

TABLE III. Fundamental vibrational frequencies (cm^{-1}) for the $\tilde{B}$ state of CH_2CFO.

Mode	PFY frequency	LIF frequency[a]
ν_3 (C–O stretch)	1794	1790
ν_4 (CHH scissor)	1412	1409
ν_5 (C–F stretch)	1255	1253
ν_6 (CH$_2$ rock)	911	911
ν_7 (C–C stretch)	876	874
ν_8 (FCO bend)	534	537
ν_9 (CCO bend)	421	421

[a]References 1 and 6.

QCISD/6-31G(d) level of theory. Additionally, the total *ab initio* energies are given in Table V at both the current level of theory and at the B3LYP/6-311G** and CCSD(T)/6-311G** levels as reported by Cao *et al.*[7] Finally, the relative energies, including the zero-point vibrational energies (ZPVE) for the QCISD/6-311G** level, can be found in Table V and are illustrated in Fig. 9. The ZPVEs have been scaled by 0.9776.[42] At the QCISD/6-311G** level of theory, the calculated dissociation energy is several hundred meV less than the experimental value given in Sec. I.

Our attempts to locate a unimolecular dissociation pathway to HF+HCCO products with either a three- or four-centered transition state at the B3LYP/6-311G** level of theory were unsuccessful. The calculations of the ground state potential energy surface of C_2H_2FO by Cao *et al.*[7] also do not include a dissociation pathway to this channel, although they reported a bimolecular transition state corresponding to $F+H_2CCO \rightarrow HF+HCCO$ direct hydrogen abstraction.

C. Translational energy distributions

In photodissociation experiments, $P(E_T)$ distributions peaking at low translational energy are often indicative of statistical dissociation following internal conversion to the ground state. Statistical decay that proceeds along a reaction coordinate that has no exit barrier with respect to products can be modeled by phase space theory[43] (PST). Here, all product states allowed by conservation of energy and angular momentum are assumed to be equally probable. The details of the application of PST to the calculation of translational energy distributions have been presented elsewhere.[44–46] Our application of PST assumes a long-range potential $V(r) = -C_0/r^6$ and harmonic vibrational levels. Figure 10 depicts the results of applying PST to the dissociation of CH_2CFO at the excitation energy corresponding to the $B \leftarrow X$ origin. There is a clear disparity between the experimental data and distributions generated by PST, solid and dashed lines, respectively. The PST distributions peak closer to $E_T=0$ and in general are much slower than the observed distributions. Thus, it appears that the conditions under which PST is valid, i.e., statistical decay with no exit barrier, do not apply to CH_2CFO dissociation.

On the other hand, the weak dependence of the observed distributions on photon energy and their peaking at translational energies well above zero are suggestive of statistical dissociation over an exit barrier. In such a process, energy is

points using the GAUSSIAN 98 program package[41] at the QCISD/6-311G** level of theory. The optimized geometries are depicted in Fig. 9 with the bond lengths, angles, and vibrational frequencies provided in Table IV. The frequencies presented in Table IV have been scaled by a factor of 0.9538 as recommended by Scott and Radom[42] for the
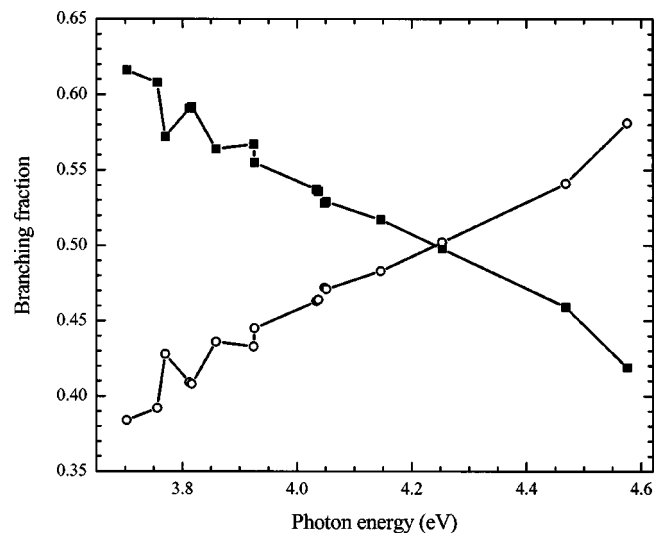

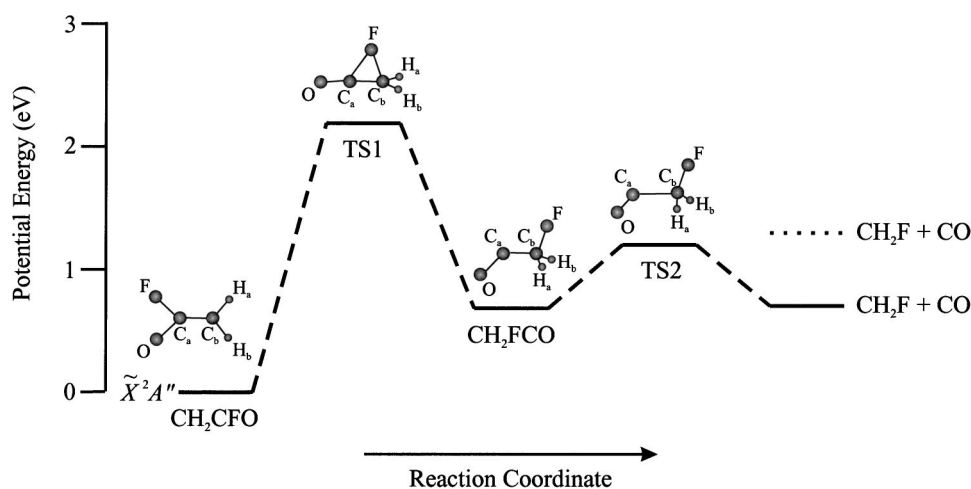FIG. 8. Branching fractions for the CH_2F+CO (■) and HCCO+HF (○) product channels.

FIG. 9. Schematic of potential energy surfaces of the CH₂CFO system. All geometries and energies indicated by solid lines have been calculated at the QCISD/6-311G** level of theory. The dotted line denotes the experimental energy of the CH₂F+CO products.

first randomized prior to encountering the barrier. Passage over the barrier then results in a rapid release of energy that is not statistically distributed, yielding a photofragment translational energy distribution that peaks at 40%–80% of the barrier height.[47,48] Assuming such a mechanism is valid, our $P(E_T)$ distributions for the CH₂F+CO and HCCO+HF channels are consistent with barrier heights between 0.63 and 1.3 eV with respect to products.

The average translational energy release for both product channels is in the range of 0.66–0.90 eV. This corresponds to 27%–30% of the available energy being partitioned into

product translation for the CH₂F+CO channel and 27%–35% for the HCCO+HF channel. The average translational energy release, $\langle E_T \rangle$, and fraction of energy released into translation, f_T, can be found in Table VI. The values of f_T presented in the current study are of comparable magnitude to those previously observed from those dissociation pathways that involve an exit barrier in vinoxy[28] and 1,3-butadiene.[49]

In order to determine an approximate barrier height consistent with our $P(E_T)$ distributions, we use the barrier im-

TABLE IV. *Ab initio* geometries and vibrational frequencies of stationary points. Bond lengths are in angstroms and frequencies are in cm⁻¹. All frequencies have been scaled by a factor of 0.9538 (Ref. 42).

CH₂CFO $\widetilde{X}\,^2A''$	CH₂FCO	TS1	TS2
		Geometries	
$r(C_aC_b)=1.451$	$r(C_aC_b)=1.533$	$r(C_aC_b)=1.346$	$r(C_aC_b)=2.081$
$r(C_aO)=1.196$	$r(C_aO)=1.183$	$r(C_aO)=1.149$	$r(C_aO)=1.149$
$r(C_aF)=1.353$	$r(C_bF)=1.369$	$r(C_aF)=2.250$	$r(C_bF)=1.342$
$r(C_bH_a)=1.083$	$r(C_bH_a)=1.096$	$r(C_bH_a)=1.080$	$r(C_bH_a)=1.089$
$r(C_bH_b)=1.083$	$r(C_bH_b)=1.096$	$r(C_bH_b)=1.080$	$r(C_bH_b)=1.089$
$\angle(OC_aC_b)=127.21°$	$\angle(OC_aC_b)=125.36°$	$\angle(OC_aC_b)=178.88°$	$\angle(OC_aC_b)=114.70°$
$\angle(FC_aC_b)=112.02°$	$\angle(FC_bC_a)=110.71°$	$\angle(FC_aC_b)=65.45°$	$\angle(FC_bC_a)=106.58°$
$\angle(H_aC_bC_a)=120.79°$	$\angle(H_aC_bC_a)=108.13°$	$\angle(H_aC_bC_a)=118.55°$	$\angle(H_aC_bC_a)=101.64°$
$\angle(H_bC_bC_a)=118.08°$	$\angle(H_bC_bC_a)=108.13°$	$\angle(H_bC_bC_a)=118.55°$	$\angle(H_bC_bC_a)=101.68°$
$\angle(OC_aC_bF)=180.0°$	$\angle(OC_aC_bF)=180.0°$	$\angle(OC_aC_bF)=179.92°$	$\angle(FC_bC_aO)=179.94°$
$\angle(H_aC_bC_aF)=0.0°$	$\angle(H_aC_bC_aF)=120.22°$	$\angle(H_aC_bC_aF)=94.73°$	$\angle(H_aC_bC_aO)=-61.31°$
$\angle(H_bC_bC_aF)=180.0°$	$\angle(H_bC_bC_aH_a)=119.56°$	$\angle(H_bC_bC_aF)=-94.88°$	$\angle(H_bC_bC_aO)=61.18°$
		Frequencies	
3172	2998	3192	3098
3052	2934	3078	2978
1715	1833	2108	1937
1415	1428	1360	1441
1215	1312	1075	1166
980	1213	974	1135
851	1095	630	982
698	870	428	516
585	815	405	309
577	491	310	182
408	308	297	64
307	129	167i	434i

TABLE V. Total *ab initio* energies of stationary points in hartree/particle. Relative energies in eV are provided in parentheses. The relative energies at the QCISD/6-311G** level of theory include the zero-point vibrational energies scaled by a factor of 0.9776 (Ref. 42).

Species	B3LYP/ 6-311G**[a]	CCSD(T)/ 6-311G**[a]	QCISD/ 6-311G**
$CH_2CFO \; \tilde{X} \, ^2A''$	−252.504 900 4 (0.0)	−251.924 597 5 (0.0)	−251.905 362 (0.0)
CH_2FCO	−252.477 660 5 (0.74)	−251.900 221 2 (0.66)	−251.880 867 (0.70)
TS1	−252.440 008 3 (1.77)	−251.843 961 3 (2.19)	−251.822 154 (2.19)
TS2	−252.454 022 1 (1.38)	−251.879 924 2 (1.22)	−251.858 816 (1.19)
CH_2F+CO	−252.458 246 1 (1.27)	−251.891 596 2 (0.90)	−251.873 602 (0.71)

[a]Reference 7.

pulsive model (BIM) developed by North *et al.*[50] This simple model predicts the average translational energy release in a dissociation process whose pathway involves a barrier. In the BIM, the total available energy is divided into a statistical reservoir and an impulsive reservoir. The statistical reservoir spans the energy from the transition state to the maximum available energy, and the energy of this region is partitioned among the product vibrational, rotational, and translational degrees of freedom following the methodology outlined by North *et al.*[50] through the use of the CH_2CFO ground state vibrational frequencies calculated at the QCISD/6-311G** level of theory (see Table IV). The impulsive reservoir represents the remainder of the available energy, namely the energy of the TS with respect to the energy of the products. The energy of this reservoir is divided between product rotational and translational degrees of freedom using a rigid impulsive model based on the TS geometry.

The decay pathway for the CH_2F+CO channel on the ground state potential energy surface has been shown to have two barriers: the isomerization barrier between CH_2CFO and CH_2FCO and that leading directly to products.[7] As shown in Table V, the isomerization transition state, TS1, has been calculated to lie approximately 2.19 eV above the ground state, or 1.48 eV above the CH_2F+CO products, while the dissociation barrier, TS2, is 1.19 eV above the ground state, or 0.48 eV above channel (1). TS1 is too high and TS2 is too low to generate $P(E_T)$ distributions peaking at 0.5 eV. However, as noted in Sec. IV B, the calculated energy of the CH_2F+CO product channel relative to CH_2CFO is lower than the experimental value. If the product energy is raised by 0.62 eV to reproduce the experimental value and all barrier heights remain unaltered, then the energy difference between TS1 and channel (1) is lowered to 0.86 eV. Note that this procedure lowers the energy of TS2 to a value less than that of channel (1); a more realistic energy correction scheme would probably reduce the TS2 barrier height relative to channel (1), but not eliminate it entirely. Regardless of the exact barrier height for TS2, adjustment of the calculated product energy yields an energy for TS1 that is within the acceptable range for the barrier governing the $P(E_T)$ distributions. Thus, the geometry for TS1 calculated at the
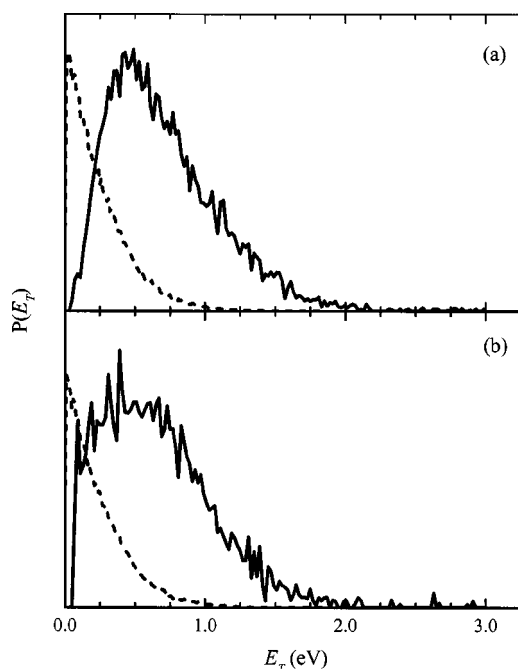

FIG. 10. Translational energy distributions for the 0_0^0 transition of the $\tilde{B} \leftarrow \tilde{X}$ band as measured experimentally (solid) and calculated from phase space theory (dashed) for the (a) CH_2F+CO and (b) HCCO+HF product channels.

TABLE VI. Average photofragment translational energies, $\langle E_T \rangle_{exp}$, and fraction of energy released into translation, f_T, for the CH_2F+CO and HCCO+HF channels. The values for $\langle E_T \rangle_{BIM}$ predicted by the barrier impulsive model for the CH_2F+CO channel are also provided. All energies are in eV.

Photon energy	CH_2F+CO			HCCO+HF	
	$\langle E_T \rangle_{exp}$	$\langle E_T \rangle_{BIM}$	f_T	$\langle E_T \rangle_{exp}$	f_T
3.703	0.71	0.77	0.30	0.66	0.35
3.756	0.71	0.77	0.29	0.67	0.35
3.770	0.74	0.78	0.30	0.68	0.35
3.812	0.72	0.78	0.29	0.66	0.33
3.816	0.73	0.78	0.29	0.66	0.33
3.859	0.75	0.79	0.30	0.67	0.33
3.924	0.74	0.79	0.29	0.66	0.32
3.926	0.75	0.79	0.29	0.68	0.33
4.034	0.77	0.81	0.28	0.69	0.31
4.037	0.77	0.81	0.28	0.68	0.31
4.048	0.78	0.81	0.29	0.69	0.31
4.051	0.78	0.81	0.29	0.69	0.31
4.146	0.80	0.82	0.28	0.70	0.30
4.253	0.82	0.83	0.28	0.69	0.29
4.468	0.85	0.86	0.27	0.74	0.28
4.575	0.90	0.87	0.28	0.75	0.27

QCISD/6-311G** level with a barrier height of 0.86 eV is used in the BIM calculation of $\langle E_T \rangle$ for the CH$_2$F+CO channel. The results, shown in Table VI, show that the barrier impulsive model predicts average photofragment translational energies that are consistent with the experimental data, supporting the proposition that the photodissociation of CH$_2$CFO to CH$_2$F+CO proceeds on the ground state potential energy surface with TS1 governing the observed $P(E_T)$ distributions.

As mentioned in the previous section, a transition state leading to HCCO+HF products from CH$_2$CFO could not be located. Without knowledge of the geometry and frequencies of the transition state leading to these fragments, application of the BIM is not feasible. Further examination of the possible dissociation mechanisms for the HCCO+HF channel is presented in the following section.

V. DISCUSSION

The results from these experiments provide new information on the excited state spectroscopy and dissociation pathways of the CH$_2$CFO radical. While the previously reported LIF excitation spectrum of CH$_2$CFO ended $\sim$2700 cm^{-1} above the origin of the $\tilde{B}\,^2A''$ state,[1] the PFY spectrum extends to $\sim$9000 cm^{-1} above the origin. The termination of the LIF spectrum at photon energies above 32 570 cm^{-1} appears not to be from quenching of the fluorescence, but rather experimental limitations that precluded scanning to higher energies. However, comparison of the intensities between the PFY and LIF excitation spectra indicate a decrease in fluorescence quantum yield with increasing photon energy, presumably owing to an increased dissociation rate.

At all photon energies used to excite the $\tilde{B}\leftarrow\tilde{X}$ transition, only CH$_2$F+CO and HCCO+HF photoproducts are observed. As indicated in Sec. IV C, the CH$_2$F+CO channel is attributed to internal conversion to the ground state followed by dissociation over an exit barrier. The results for the HCCO+HF channel are, at first glance, also consistent with ground state dissociation over a barrier. If decay to channel (2) is the result of overcoming a larger barrier with respect to the ground state of CH$_2$CFO than that leading to channel (1), TS1, then the CO-loss channel would dominate at lower photon energies. Furthermore, if the vibrational frequencies for this transition state are lower than those of TS1, then channel (2) will become favored as the photon energy is increased. This overall trend is indeed observed (see Fig. 8). Dissociation to this channel from CH$_2$CFO would presumably involve passage through a four-center transition state, while dissociation from the higher energy CH$_2$FCO isomer could occur via a three-center transition state. However, we were unable to locate either TS in our electronic structure calculations. While HCCO+HF products are seen as a minor channel in the F+CH$_2$CO reaction,[17–19] these products were attributed to a direct hydrogen abstraction mechanism rather than dissociation via a long-lived intermediate; the corresponding bimolecular transition state (which was found in both our calculations and those of Cao *et al.*[7]) cannot be accessed from the ground state of CH$_2$CFO.

One must therefore consider the possibility that channel

(2) results from dissociation on the $\tilde{A}$ state of CH$_2$CFO, following internal conversion from the $\tilde{B}$ to the $\tilde{A}$ state. If the mechanism by which CH$_2$F+CO products are generated also involves IC to the $\tilde{A}$ state, then the competition between dissociation to channel (2) and IC from the $\tilde{A}$ to the $\tilde{X}$ state will dictate the product branching ratios. On the other hand, if dissociation to CH$_2$F+CO involves direct internal conversion from the $\tilde{B}$ to the $\tilde{X}$ state, then the competition between the two IC pathways will govern the branching ratios.

As discussed in Sec. IV C, comparison of the observed average translational energy release for channel (1) to that predicted by the barrier impulsive model supports a dissociation mechanism in which the $P(E_T)$ distributions are determined by the isomerization barrier at TS1. An analogous decay pathway was proposed in the dissociation of vinoxy to CH$_3$+CO photofragments.[28] In both cases, the much lower barrier at TS2 does not appear to influence the translational energy distributions significantly. However, the internal conversion pathway between the $\tilde{X}$ and $\tilde{B}$ states is likely different for the two radicals. Based on the sharp increase in vinoxy dissociation at photon energies greater than 1400 cm^{-1} above the origin, and calculations of stationary points[28] and potential energy curves along the C–C torsional coordinate,[30] the rapid mechanism $\tilde{B}\,^2A''\rightarrow\tilde{A}\,^2A'\rightarrow\tilde{X}\,^2A''$ was proposed as the internal conversion pathway for vinoxy.[28] This mechanism was recently corroborated and elaborated upon by Matsika and Yarkony.[31]

In contrast to vinoxy, CH$_2$CFO exhibits neither a sharp increase in dissociation versus fluorescence, nor a mode-specific enhancement of dissociation. Furthermore, the angular distributions for both channels (1) and (2) were found to be isotropic at all excitation energies employed; anisotropic angular distributions were observed from the dissociation of vinoxy at photon energies in excess of 1400 cm^{-1} above the origin.[28] Thus, the decay mechanism for CH$_2$CFO follows a slower pathway than that of vinoxy and is not influenced by the vibrational mode excited. These results are consistent with calculations by Yamaguchi *et al.*[3] that show the torsional mode in the $\tilde{B}$ state of CH$_2$CFO to be much stiffer than in vinoxy, implying that this mode does not provide a facile, mode-specific gateway to internal conversion and dissociation in CH$_2$CFO.

Interestingly, we do not observe the C–F bond fission channel, CH$_2$CO+F, which is equivalent to the dominant H-loss channel in vinoxy. While channel (4) cannot be detected in the current experiments, generation of CHFCO+H is unlikely. The pathway along the ground electronic state leading to these products first involves the isomerization of CH$_2$CFO to CH$_2$FCO, as in the generation of CH$_2$F+CO products, and then passage over barriers significantly higher than that leading to channel (1).[7]

VI. CONCLUSIONS

The current work presents the photodissociation spectroscopy and dynamics of the CH$_2$CFO radical following excitation of the $\tilde{B}\,^2A''\leftarrow\tilde{X}\,^2A''$ transition. CH$_2$CFO has been found to predissociate from 29 870 to 38 800 cm^{-1}. Obser-

vation of the $\tilde{B}$ band above 32 570 cm^{-1} has not been previously reported, and several assignments of vibrational features within this new region have been made. At all photon energies employed, CH$_2$F+CO and HCCO+HF are the sole fragment channels present with the branching ratio between the two channels shifting from predominantly CH$_2$F+CO to HCCO+HF as the excitation energy is increased. The decay mechanisms leading to both product channels involve internal conversion from the $\tilde{B}$ state as well as an exit barrier to dissociation. Comparison of the average photofragment translational energy to that predicted by the barrier impulsive model indicates that the CH$_2$F+CO channel results from fragmentation on the ground state with the $P(E_T)$ distributions influenced primarily by the isomerization barrier between CH$_2$CFO and CH$_2$FCO. The mechanism for the HCCO+HF channel is less clear, involving dissociation either on the ground state or the excited $\tilde{A}$ state of CH$_2$CFO.

ACKNOWLEDGMENTS

[1] M. Furubayashi, I. Bridier, S. Inomata, N. Washida, and K. Yamashita, J. Chem. Phys. **106**, 6302 (1997).
[2] S. A. Wright and P. J. Dagdigian, J. Chem. Phys. **107**, 9755 (1997).
[3] M. Yamaguchi, M. Furubayashi, S. Inomata, and N. Washida, Chem. Phys. Lett. **298**, 93 (1998).
[4] S. Inomata, M. Yamaguchi, and N. Washida, J. Chem. Phys. **116**, 6961 (2002).
[5] S. Inomata, I. Bridier, M. Furubayashi, T. Imamura, G. Inoue, M. Yamaguchi, and N. Washida, J. Phys. Chem. **105**, 7559 (2001).
[6] S. Inomata, M. Furubayashi, T. Imamura, N. Washida, and M. Yamaguchi, J. Chem. Phys. **111**, 6356 (1999).
[7] D. B. Cao, Y. H. Ding, Z. S. Li, X. R. Huang, and C. C. Sun, J. Phys. Chem. **106**, 8917 (2002).
[8] M. W. Chase and National Institute of Standards and Technology (U.S.), *NIST-JANAF Thermochemical Tables*, 4th ed. (American Chemical Society, American Institute of Physics for the National Institute of Standards and Technology, Washington, D.C., 1998).
[9] B. Ruscic, A. F. Wagner, L. B. Harding, R. L. Asher, D. Feller, D. A. Dixon, K. A. Peterson, Y. Song, X. M. Qian, C. Y. Ng, J. B. Liu, and W. W. Chen, J. Phys. Chem. A **106**, 2727 (2002).
[10] W. B. DeMore, S. P. Sander, D. M. Golden, R. F. Hampson, M. J. Kurylo, C. J. Howard, A. R. Ravishankara, C. E. Kolb, and M. J. Molina, *Chemical Kinetics and Photochemical Data for use in Stratospheric Modeling* (NASA, JPL, California Institute of Technology, Pasadena, 1997).
[11] D. L. Osborn, D. H. Mordaunt, H. Choi, R. T. Bise, D. M. Neumark, and C. M. Rohlfing, J. Chem. Phys. **106**, 10087 (1997).
[12] B. Ruscic, M. Litorja, and R. L. Asher, J. Phys. Chem. A **103**, 8625 (1999).
[13] V. M. Orlov, A. A. Krivoruchko, A. D. Misharev, and V. V. Takhistov,

[14] Bull. Acad. Sci. USSR Div. Chem. Sci. **35**, 2404 (1986).
R. Faird and T. B. Mcmahon, Can. J. Chem. **58**, 2307 (1980).
[15] J. B. Pedley, R. D. Naylor, and S. P. Kirby, *Thermochemical Data of Organic Compounds*, 2nd ed. (Chapman and Hall, New York, 1986).
[16] J. Marks, J. E. Brauman, R. D. Mead, K. R. Lykke, and W. C. Lineberger, J. Chem. Phys. **88**, 6785 (1988).
[17] J. W. Hudgens, C. S. Dulcey, G. R. Long, and D. J. Bogan, J. Chem. Phys. **87**, 4546 (1987).
[18] J. Ebrecht, W. Hack, and H. G. Wagner, Ber. Bunsenges. Phys. Chem. **94**, 587 (1990).
[19] J. Grussdorf, J. Nolte, F. Temps, and H. G. Wagner, Ber. Bunsenges. Phys. Chem. **98**, 546 (1994).
[20] K. Sung and T. T. Tidwell, J. Org. Chem. **63**, 9690 (1998).
[21] H. E. Hunziker, H. Kneppe, and H. R. Wendt, J. Photochem. Photobiol., A **17**, 377 (1981).
[22] T. Gejo, M. Takayanagi, T. Kono, and I. Hanazaki, Chem. Lett. **1993**, 2065 (1993).
[23] G. Inoue and H. Akimoto, J. Chem. Phys. **74**, 425 (1981).
[24] L. F. Dimauro, M. Heaven, and T. A. Miller, J. Chem. Phys. **81**, 2339 (1984).
[25] R. L. Wan, X. R. Chen, F. Wu, and B. R. Weiner, Chem. Phys. Lett. **260**, 539 (1996).
[26] L. R. Brock and E. A. Rohlfing, J. Chem. Phys. **106**, 10048 (1997).
[27] H. Nagai, R. T. Carter, and J. R. Huber, Chem. Phys. Lett. **331**, 425 (2000).
[28] D. L. Osborn, H. Choi, D. H. Mordaunt, R. T. Bise, D. M. Neumark, and C. M. Rohlfing, J. Chem. Phys. **106**, 3049 (1997).
[29] L. S. Alconcel, H. J. Deyerl, V. Zengin, and R. E. Continetti, J. Phys. Chem. **103**, 9190 (1999).
[30] M. Yamaguchi, Chem. Phys. Lett. **221**, 531 (1994).
[31] S. Matsika and D. R. Yarkony, J. Chem. Phys. **117**, 7198 (2002).
[32] A. A. Hoops, J. R. Gascooke, A. E. Faulhaber, K. E. Kautzman, and D. M. Neumark, Chem. Phys. Lett. **374**, 235 (2003).
[33] D. J. Leahy, D. L. Osborn, D. R. Cyr, and D. M. Neumark, J. Chem. Phys. **103**, 2495 (1995).
[34] R. E. Continetti, D. R. Cyr, D. L. Osborn, D. J. Leahy, and D. M. Neumark, J. Chem. Phys. **99**, 2616 (1993).
[35] D. L. Osborn, D. J. Leahy, D. R. Cyr, and D. M. Neumark, J. Chem. Phys. **104**, 5026 (1996).
[36] A. N. Nesmejanow and E. J. Kahn, Chem. Ber. **67**, 370 (1934).
[37] J. M. B. Bakker, J. Phys. E **6**, 785 (1973).
[38] J. M. B. Bakker, J. Phys. E **7**, 364 (1974).
[39] Z. Amitay and D. Zajfman, Rev. Sci. Instrum. **68**, 1387 (1997).
[40] R. N. Zare, Mol. Photochem. **4**, 1 (1972).
[41] M. J. Frisch, G. W. Trucks, H. B. Schlegel *et al.*, GAUSSIAN 98, Revision A.9, Gaussian, Inc., Pittsburgh, PA, 1998.
[42] A. P. Scott and L. Radom, J. Phys. Chem. **100**, 16502 (1996).
[43] P. Pechukas and J. C. Light, J. Chem. Phys. **42**, 3281 (1965).
[44] P. Pechukas, J. C. Light, and C. Rankin, J. Chem. Phys. **44**, 794 (1966).
[45] P. J. Robinson and K. A. Holbrook, *Unimolecular Reactions* (Wiley-Interscience, New York, 1972).
[46] H. Choi, R. T. Bise, A. A. Hoops, D. H. Mordaunt, and D. M. Neumark, J. Phys. Chem. A **104**, 2025 (2000).
[47] A. M. Wodtke, E. J. Hintsa, and Y. T. Lee, J. Phys. Chem. **90**, 3549 (1986).
[48] X. S. Zhao, R. E. Continetti, A. Yokoyama, E. J. Hintsa, and Y. T. Lee, J. Chem. Phys. **91**, 4118 (1989).
[49] J. C. Robinson, S. A. Harris, W. Z. Sun, N. E. Sveum, and D. M. Neumark, J. Am. Chem. Soc. **124**, 10211 (2002).
[50] S. W. North, D. A. Blank, J. D. Gezelter, C. A. Longfellow, and Y. T. Lee, J. Chem. Phys. **102**, 4447 (1995).